ADVANCED ENERGY & SUSTAINABILITY RESEARCH
Open Access
www.advenergysustres.com

Synthesis of Doped g-C_3N_4 Photonic Crystals for Enhanced Light-Driven Hydrogen Production from Catalytic Water-Splitting

Simon Y. Djoko T., Sunil Kwon, Prasenjit Das, Vincent Weigelt, Warisha Tahir, Babu Radhakrishnan, Klaus Schwarzburg, Arne Thomas, Michael Schwarze, and Reinhard Schomäcker*

Dopants are frequently used to improve graphitic carbon nitride (gCN) photoactivity. As a doping source, phosphomolybdic acid (PMA) can activate doping sites inside the gCN lattice, resulting in 2D Mo:P-gCN porous material. However, the gradual loading of the PMA fraction has no systematic improvement in the Mo:P-gCN photoactivity. For improving the optoelectronic properties of Mo:P-gCN, its textural geometry is a controllable parameter that can provide enhanced photonic properties, achievable by shaping its morphology through a crystalline template structure, namely, photonic crystals (PCs). Herein, a doped PC material is made of Mo:P-gCN and PCs and labeled as Mo:P-gCN/PCs. The impact of PCs is highlighted in the structural, electronic, and optical performances of Mo:P-gCN. A well-defined 3D crystalline network is evidenced by microscopic measurements (scanning electron microscopy, AFM, focused ion beam). Mo:P-gCN/PCs shows a hydrogen production rate (750 µmol g^{-1} h^{-1}) one time higher than Mo:P-gCN and 6 times higher than pure gCN. The synthesis strategy proposed in this work leads simultaneously to the Mo:P codoping effect provided by PMA and the slow photon effect due to the PC structure, offering a novel strategy to improve the gCN photoactivity by simultaneously applying polyoxometalates as modifiers and polystyrene opals as templates.

1. Introduction

When used as a catalyst for light-driven reactions, graphitic carbon nitride (gCN) exhibits low performance due to the slow charge separation and fast recombination. Still, it can be used as a chemical framework to synthesize highly efficient catalyst materials to enhance light harvesting.[1–3] Thus, several approaches, including using dopants, have been undertaken to narrow the bandgap of gCN and mitigate charge recombination, substantially improving its catalytic performances.[4] Several studies have shown that compounds containing phosphorus, such as nickel phosphide,[5] molybdenum phosphide,[6–8] phosphomolybdic acid (PMA),[7] and hypophosphite monohydrate,[9] can improve the electronic properties of gCN when they are used as precursors to promote the doping phenomenon. Unfortunately, these doping materials do not allow the modified gCN to achieve the highest quantum efficiency for the hydrogen evolution reaction (HER) during the photocatalytic water-splitting reaction.[10] To some extent, it has been demonstrated that other metal cluster compounds from the polyoxometalate (POM) family not only provide a pronounced doping effect but also help to give heterohybridizations and structural defects in the final catalyst.[10] Whatever the doping capability the promotor material exhibits, controlling the doping selectivity to improve the electronic properties remains challenging.

The textural geometry is a controllable parameter that could also give Mo:P-gCN a 3D-oriented porous structure with

S. Y. Djoko T., S. Kwon, M. Schwarze, R. Schomäcker
Department of Chemistry
Multiphase Reaction Engineering
Technische Universität Berlin
TC8, Straße des 17. Juni 124, 10623 Berlin, Germany
E-mail: Michael.schwarze@tu-berlin.de

The ORCID identification number(s) for the author(s) of this article can be found under https://doi.org/10.1002/aesr.202400181.

DOI: 10.1002/aesr.202400181

P. Das, V. Weigelt, W. Tahir, A. Thomas
Department of Chemistry
Technische Universität Berlin
Functional Materials, BA216 Hardenbergstr. 40, 10623 Berlin, Germany

B. Radhakrishnan, K. Schwarzburg
Institute for Solar Fuels,
Helmholtz-Zentrum Berlin für Materialien und Energie GmbH
Hahn-Meitner-Platz 1, 14109 Berlin, Germany

exceptional dielectric and optoelectronic properties. This helps ensure the desired band transitions and avoid the undesired ones. By definition, photonic crystal (PC) materials based on inverse opal structures (IOS) are periodic dielectric structures designed to form the energy band structure for photons, allowing or forbidding the propagation of electromagnetic waves of specific frequency ranges, making them ideal for light harvesting applications.[11,12] They were first proposed by Bykov[13] in 1972, and it was suggested that electron–hole radiative recombination would be severely inhibited for a 3D periodic dielectric structure with an electromagnetic bandgap overlapping the electronic bandgap. The photonic bandgap (PBG) of PCs can be tuned to specific wavelengths, forming regions where the light propagation with certain frequencies is forbidden and slow near its stop band, resulting in radiative multiple scattering.[14,15] Such a slow-light effect combined with other material features can considerably increase the effective optical path, leading to photon delay and light confinement in PC-based materials. These attractive properties exhibited by the PCs have been widely used for practical applications such as sensors and solar cells and are also appealing for photocatalysis.[14–17] Considering these advantages, it is believed that combining the enhanced electronic properties of Mo:P-doped gCN with the PBG properties of PCs would significantly contribute to the enhancement of the light harvesting

In this study, we have fabricated a PC material out of Mo:P-doped gCN for the first time. These PCs have been applied as photocatalysts, showing efficient light harvesting and charge separation in photo-electrocatalytic and photocatalytic sunlight energy conversion. Suspended polystyrene (PS) spheres were used as a template to prepare the desired PC structure. PMA was a doping source to prepare Mo:P-doped gCN. Simon et al.[10] used PMA as a P-doping source to improve the electronic properties of gCN, which resulted in enhanced photocatalytic performances. However, despite the successful doping of P atoms and the in situ incorporation of Mo ions, the final Mo:P-doped gCN performances were not satisfactory to compete with other CN-based materials. Thus, in this study, the bulk gCN/PMA composite was prepared following the reported procedure[10] and it was used as the precursor of the PC generation. The synthesis strategy leads to a new material with simultaneously improved electronic properties (from the Mo:P-doping effect) and optical properties (from the slow photon effect of its PBG). Both properties lead to a remarkable enhancement of the photocatalytic performance during light-driven hydrogen evolution. For comparison, pure gCN-based PCs were prepared, and their photocatalytic activities were compared to those of Mo:P-gCN/PCs. The effect of the PS template agent was demonstrated by preparing the equivalent PS-free material labeled as gCN and Mo:P-gCN. This work offers a simple strategy to simultaneously provide a doping effect and slow PBG effect in a single-component material, resulting in the better enhancement of light harvesting and reduced charge recombination. It could be applied to designing highly efficient photocatalytic systems like artificial leaves to achieve artificial photosynthesis for better solar-to-energy conversion efficiency.

2. Synthesis of PCs (Mo:P-gCN/PCs Powders and FTO-immobilized)

The synthesis of P-doped gCN-based PCs consisted of two or three steps depending on the final requested state of the material, as shown in **Figure 1**. The gCN/PMA composite, the precursor of Mo:P-gCN/PCs, must be prepared earlier. The bulk gCN/PMA composite precursor was obtained from pure gCN and PMA through a reported solvothermal synthesis procedure.[10] The PMA was used in the former study as the doping source, and it has already been proven to boost the photoactivity of gCN.[10] The synthesis procedure of the gCN/PMA composite is well described in the Supplementary Information (SI).

Once the gCN/PMA composite is readily prepared, Mo:P-gCN/PCs powder state samples are obtained through a chemical vacuum-assisted impregnation method in colloidal suspension by mixing alkoxide gCN/PMA composite (2 mL, see SI for the gCN/PMA Alkoxide preparation) into a vial containing PS template solution (30 µL) suspended in ethanol (1 mL). After 10–15 min of gentle mechanical shaking, the obtained pale yellow colloidal mixture was transferred to the desiccator connected to a vacuum pump. Then, 20–30 min of vacuum was applied up to 40 mbar along the wet impregnation process to force the bulk gCN/PMA precursor to permeate the void spaces between the colloidal close-packed PS spheres. The vials containing the colloidal suspension mixture were then transferred to 15 min centrifugation at 8 500 rpm to accelerate the decantation process and collect the pale-yellow sludge back. The sludge was dried overnight in an air atmosphere at room temperature, and then at 60 °C for about 6–7 h to obtain the close-packed crystal composite gCN/PMA@PS. Subsequently, the P-doped gCN-based PCs were then obtained as inverse opals by removing the PS spheres template from the close-packed crystal composite gCN/PMA@PS and the resulting powder material was labeled as Mo:P-gCN/PCs (Figure 1a). The PS spheres removal was proceeded by annealing the close-packed gCN/PMA@PS into a muffle furnace at 450 °C for 2 h at a raping rate of 5 °C min^{-1} under an argon atmosphere. For comparison, pure gCN-based PCs were prepared following the same procedure by replacing the gCN/PMA precursor composite with the pure gCN to derive the close-packed gCN@PS crystal. After PS removal by thermal annealing in the same conditions mentioned above, the derivate powder PCs were obtained and labeled as gCN-PCs (Figure S1a, Supporting Information).

For photoelectrochemical (PEC) applications, the Mo:P-gCN/PCs film immobilization is required to get the PEC setup well assembled. Therefore, glasses-coated fluorine-doped tin oxide (FTO) was used as substrates on which the 3D ordered Mo:P-gCN/PCs structures were grown. Mo:P-gCN/PCs film immobilization was achieved in three steps, as described in Figure 1b. The first step consisted of the PS sphere assembly onto FTO substrates. Herein, the evaporation-assisted self-assembly method via vertical deposition allowed a well-controlled and uniform deposition of colloidal PS particles driven by lateral capillary forces.[14,15,17–19] This results in multilayered opal array films of highly ordered and closely packed spheres that would be used further as the template of the desired IO. The FTO substrates were placed vertically (35–40° concerning the vertical plan) inside

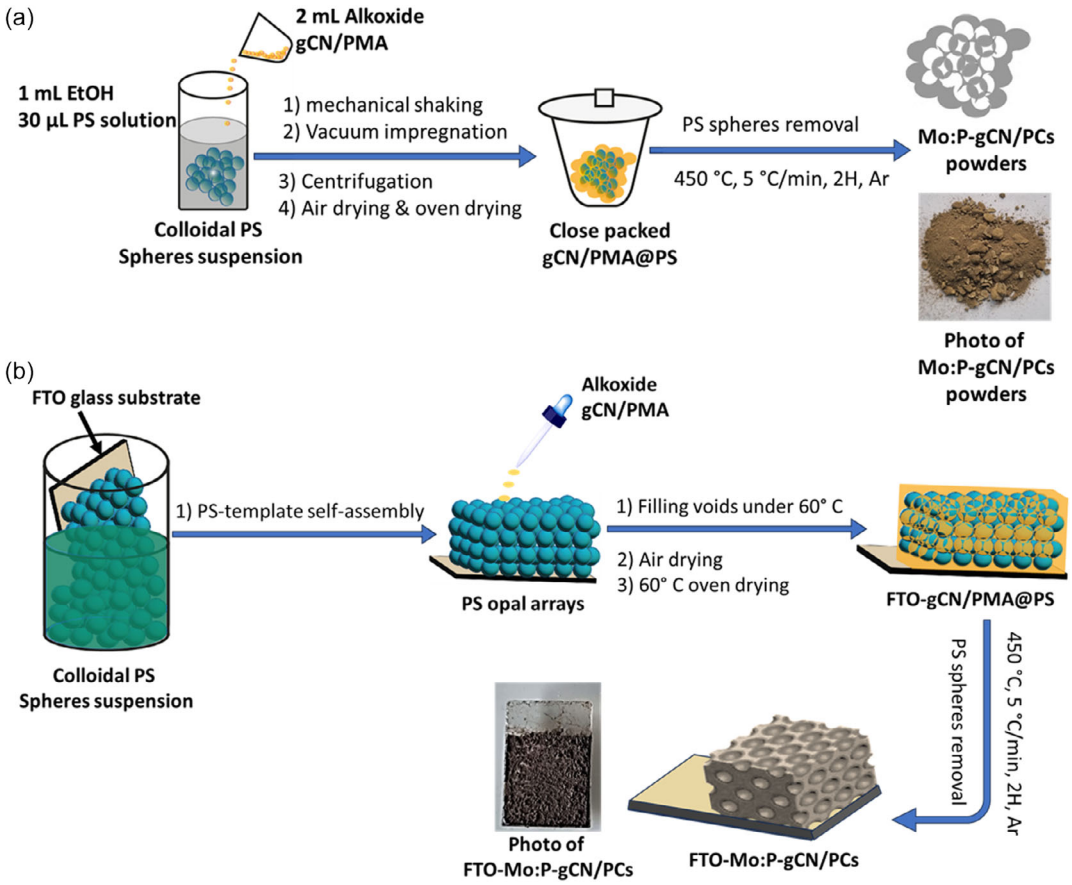

Figure 1. Schematic illustration of the PCs synthesis pathways for: a) Mo:P-gCN/PCs powders and b) FTO-Mo:P-gCN/PCs.

a vial glass containing 1% colloidal PS in an aqueous solution and kept in an oven at about 39–40 °C to allow the slow-down evaporation-assisted self-assembly.[14,15,18,19] The second step consists of the void filling of the close-packed PS with the bulk gCN/PMA precursor. The gCN/PMA alkoxide solution was initially prepared for easier drop-coating (see SI for gCN/PMA alkoxide preparation). By drop-coating under 60 °C heating, the alkoxide precursor infiltrated the voids of the PS spheres template through capillary forces. The drop-coating was repeated (6–9 times) after drying each previous layer and stopped once the gCN/PMA precursor fully recovered the FTO surface. ≈1.5–2 mL of alkoxide gCN/PMA precursor was estimated enough to get optimal void permeability and fully recover 1 cm^2 FTO substrate; the resulting close-packed crystal was labeled as FTO-gCN/PMA@PS. The third step consists of PS removal. This was carried out by thermal annealing of FTO-gCN/PMA@PS following the same conditions in the powder Mo:P-gCN/PCs synthesis procedure. The final immobilized material was labeled as FTO-Mo:P-gCN/PCs. The detailed procedure for the FTO-Mo:P-gCN/PCs film immobilization is well described in the Supporting Information (SI). For comparison, pure gCN-based PCs films were also immobilized on FTO substrates following the same procedure by replacing the gCN/PMA precursor composite with the pure gCN to derive the close-packed FTO-gCN@PS crystal. After PS removal by the thermal annealing (decomposition of PS) in the same conditions mentioned above, the derivate PCs film was obtained and labeled as FTO-gCN/PCs (Figure S1b, Supporting Information).

3. Results and Discussion

3.1. SEM, AFM, TEM, EDX, and EDS Analysis

When synthesizing PC structures, microscopic analysis is considered the most important analytical technique that helps investigate the geometrical structure and reveal the occurrence of inverse opal lattices. Scanning electron microscopy (SEM) was used to prove the occurrence of a 3D hexagonal porous structure. The temperature of the self-assembly process, the concentration of the PS spheres template, the amount of precursor, and the FTO surface area are important factors that need to be considered to achieve a well-defined and 3D-oriented IOS. **Figure 2**a,b shows SEM images for 30 and 60 µL of self-assembled PS spheres ($\phi \simeq 250$ nm), describing the best situation that might be much more favorable for forming well-defined and 3D-oriented PCs. Figure 2a demonstrates that 1% of colloidal PS in an aqueous solution is suitable enough to provide a PS sphere population required for covering 1 cm^2 FTO surface following an orderly stacking and carefully disposed arrangement in well-defined directions, forming a compact and sufficiently

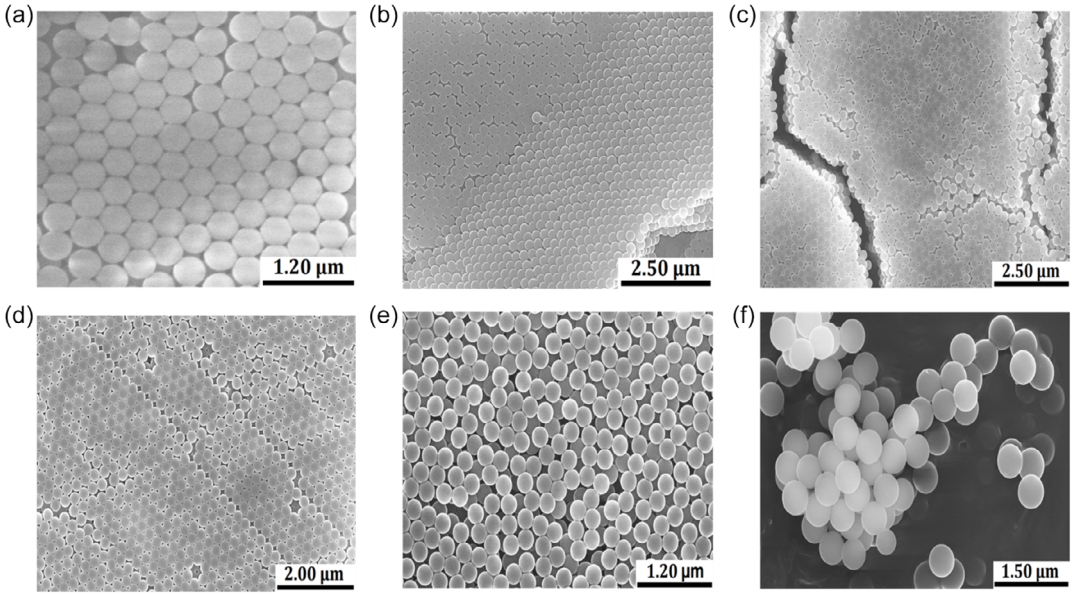

Figure 2. SEM images of PS spheres lattice obtained from a) self-assembly process with 1% colloidal PS solution, b) self-assembly process with 2% colloidal PS solution, c) self-assembly process at 60 ° C, d) self-assembly process at 37 ° C in water, e) self-assembly process at 37 ° C in methanol, and f) free-FTO self-assembly process for powder samples.

aerated 3D crystalline network resulting from the correct and coordinated positioning of the opals with each other. This situation is more required for preparing close-packed crystal arrays with a high degree of ordering and face-centered cubic (fcc) arrangement that is favorable for forming delicate IOS.[20] In this situation, the spheres are in point contact with each other, displaying several voids in 3D orientation in the crystalline opal array whereby the precursor would penetrate by capillary force to provide layers uniformly filled on the FTO surface. As a result, after PS removal, a 3D ordered hexagonal porous and close-packed array structure will be obtained, which will then be considered as IOS or PCs from the corresponding precursor. Figure 2b demonstrates that 2% of colloidal PS provides an aqueous solution saturated in the PS spheres population, and as a result, the FTO surface would be highly overloaded, and the crystalline 3D opals lattice would exhibit fewer voids that the precursor for the formation of the corresponding IOS would have filled. Although a well-defined 3D opal array is formed, this situation is unfavorable for creating solid and uniform IOS after PS removal from the FTO surface. In fact, at PS concentrations higher than 1%, the electrostatic attractive forces between PS spheres are too intense, and it would result in higher collision forces between them. Thus, the opal spheres will be highly tightly packed together so that the voids will be few, and those available will be inaccessible or hardly accessible by the precursor. A prolonged evaporation-assisted self-assembly process enables a stable, uniform, close-packed opal sphere lattice. This helps to obtain an orderly arrangement of opal spheres and to prevent any cracking structure on the FTO surface. A stable temperature and the nature of the solvent are also two main parameters that need to be controlled to achieve this requirement better. Figure 2c illustrates the cracking formation and the weak alignment of the close-packed opals structure when the self-assembly process is carried out at 60 °C with water as the solvent. Figure 2d illustrates the perfect situation to obtain a well-defined and uniform IOS. This situation corresponds to a self-assembly process performed at about 39–40 °C with water as the solvent. This results in a well-stacked, diagonal alignment of opal spheres following a 3D orientation. With another solvent like methanol, the self-assembly process goes much faster, resulting in a disorderly stacking of opal spheres on the FTO surface (Figure 2e). The easier way to prepare disorder-orientated 3D IOS was by making powder material, i.e., without any FTO substrate. This is through a free-FTO closed-packed PS spheres template, as illustrated in Figure 2f. Thus, depending on how the final IOS should look, the surface distribution, the morphology, and the geometry of the assembled opal spheres lattice are the crucial factors that directly affect the IOS assembly and hence need to be controlled. The template formation is the foundation of well-defined 3D PCs. Failing this step would lead to the failure of the final structure.

However, getting a well-defined 3D opal sphere crystal lattice as a PC template is insufficient to form a uniform hexagonal porous 3D structure. In addition to achieving well-assembled and well-defined 3D opal spheres, one should also consider the physical and chemical properties of the precursor material from where the corresponding IOS should be obtained. This parameter is significant because it directly affects the final PCs' morphology, geometry, and physical and chemical properties. To get excellent powder PCs or immobilized PCs, the precursor should be able to penetrate enough between the voids created by the close-packed PS template spheres (for immobilized PCs, see **Figure 3**a), or the PS template spheres should be able to nucleate and agglomerate enough at the precursor surface (for powder PCs, see Figure 3b,e).

Whatever the case is, an excellent affinity between the precursor and the template spheres is required. For the powder PCs, the

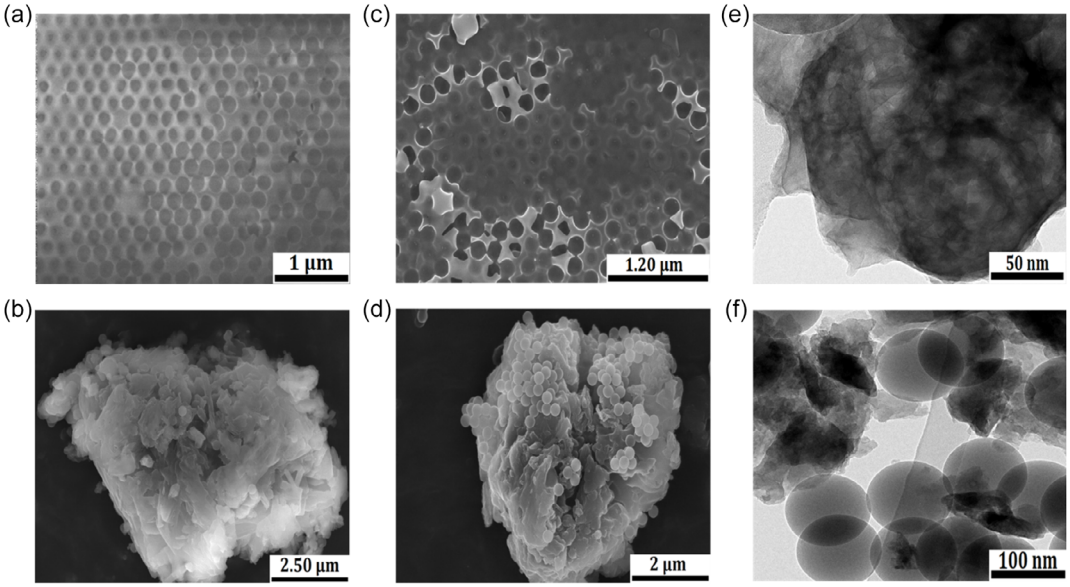

Figure 3. a–d) SEM images: FTO-gCN/PMA@PS (a), gCN/PMA@PS powder (b), FTO-gCN@PS (c), and gCN@PS powder (d). e,f) TEM images: gCN/PMA@PS powder (e) and gCN@PS powder (f).

strong penetration force applied by the vacuum is insufficient to provide this affinity. As the surface of opals is very hydrophilic and capable of forming numerous hydrogen bonds, the surface of the precursor should also exhibit good hydrophilicity in favor of the opal spheres; as a result, this situation would provide a good adhesion between the precursor surface and the PS spheres, and hence a good wetting condition (Figure 3a,b,e). Once the affinity suits well between both components (PS and precursor), attractive electrostatic forces occur in the milieu, resulting in the simultaneous occurrence of nucleation and nuclei aggregation enveloping the surface of precursor particles. As far as the PC precursor used in this study is a gCN/PMA composite made up of gCN and PMA, the higher hydrophilicity with PS spheres has been achieved by forming a chemically stable semisolid colloidal suspension, evenly mixed with appropriate solvents, and used as alkoxide. The choice of solvent is essential to fulfill this requirement. This study used H_2O_2 (30%wt), DW, and EtOH to prepare an evenly mixed and stable alkoxide gCN/PMA composite. The preparation of alkoxide gCN/PMA and the formation of sol–gel are well described in the SI. It has been found that the fraction of PMA in the gCN/PMA composite plays a vital role in the hydrophilicity of the final composite. Figure 3a–d shows SEM images of immobilized and powdered close-packed gCN@PS crystal and close-packed gCN/PMA@PS crystal composites, illustrating the wetting condition and the affinity that the precursor surface should fulfill for enhancing higher hydrophilicity with PS spheres. Figure 3a,b demonstrates that the gCN/PMA surface is well compatible for hydrophilicity and a strong affinity with PS opals, which is impossible with the gCN surface (Figure 3c,d). This phenomenon is also evidenced by the transmission electron microscopy (TEM) image of each close-packed crystal composite (Figure 3e,f). Figure S2, Supporting Information, better supports the observation of this phenomenon, and Figure S3, Supporting Information, describes the hydrophilicity of the precursor against the PS opals. It has been found that the precursor gCN/PMA composite with 1.5 g PMA loaded is more compatible with a perfect nucleation and nuclei aggregation of PS spheres on its surface due to an electrostatic environment suitable for higher hydrophilicity (Figure 3a). Then, the gCN/$PMA_{1.5}$ precursor composite with average particle $\phi = 3.2$ nm and average pore volume of 0.049 $cm^3\,g^{-1}$ ($S_{BET} = 3.0\,m^2g^{-1}$) displays the best hydrophilic condition for enhancing the PS nucleation and nuclei aggregation on its surface. Hence, this study has used it as a precursor following the simplified notation gCN/PMA (unless specified) for preparing Mo:P-gCN/PCs powders and FTO-Mo:P-gCN/PCs. Less or no nucleation and nuclei aggregation were observed on the surface of the gCN precursor (Figure 3f and S2, Supporting Information) due to the higher hydrophobicity exhibited on its surface.

After PS spheres removal from close-packed gCN@PS and close-packed gCN/PMA@PS crystal composites by thermal annealing, the final 3D ordered hexagonal porous and close-packed array structures are obtained, and their SEM and TEM images are shown in **Figure 4**. As compared to gCN/PCs (Figure 4c,d), the prior incorporation of PMA to gCN structure for the gCN/PMA precursor formation not only has a positive effect on the size of the PCs array but also affects the texture and crystallinity of the final Mo:P-gCN/PCs array (Figure 4a,b). The pores of FTO-Mo:P-gCN/PCs (Figure 4b) are well arranged in an fcc arrangement and connected to the neighboring pores by the contact point created by PS spheres, indicating that the spherical pores in that sample are also 3D ordered in a hexagonal close-packed array like the PS spheres array. Similar observations were already found with PCs made from other precursors.[16,21–23] Compared with the PS particle sizes, the FTO-Mo:P-gCN/PCs pore size is about 170 nm, indicating a significant volume shrinkage of about 68% originated from the thermal annealing (PS removal) and the sol–gel formation.

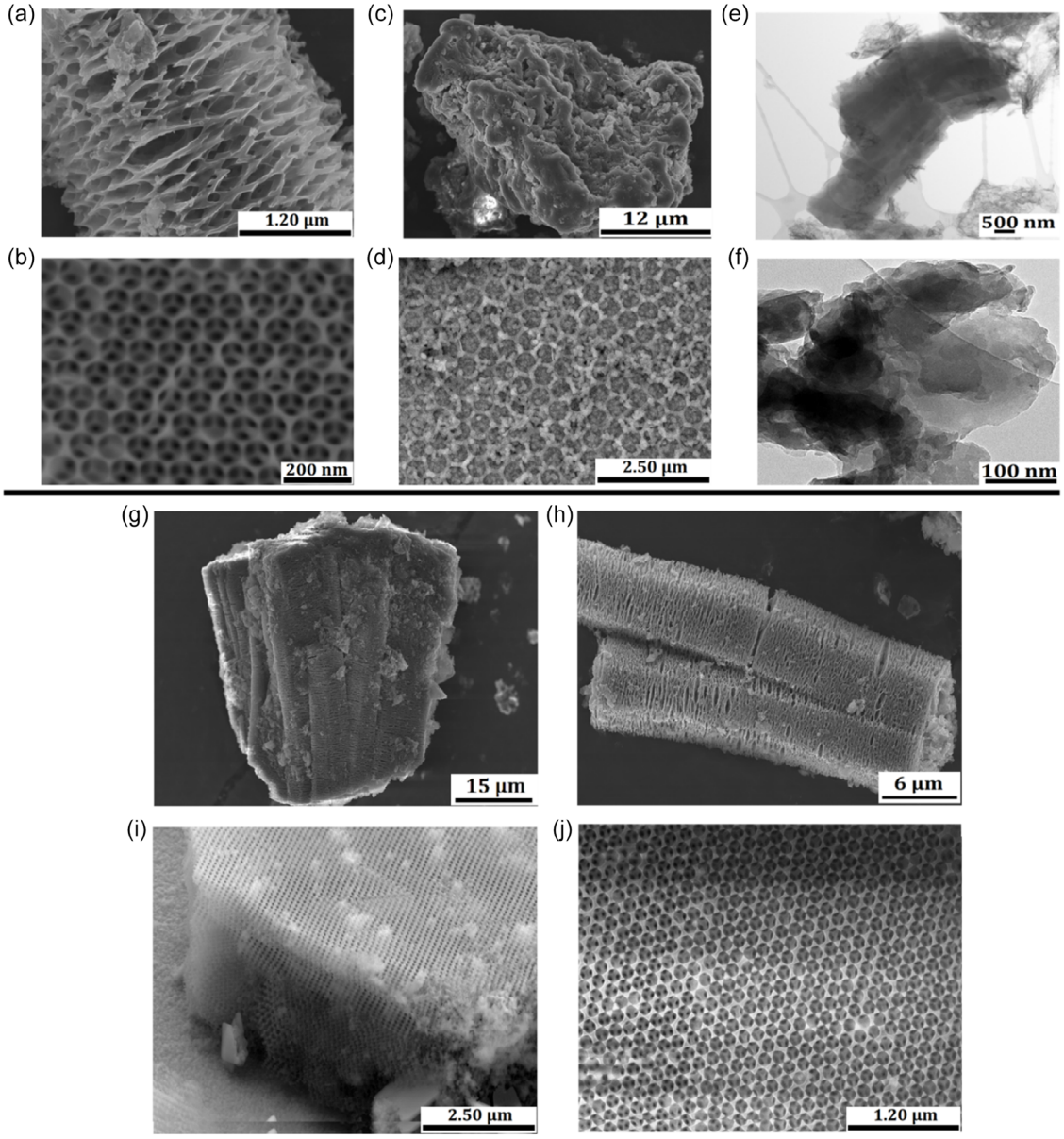

Figure 4. a–d, g–i) SEM images: Mo:P-gCN/PCs powder (a,g,h), FTO-Mo:P-gCN/PCs (b,i,j), gCN/PCs powder (c), and FTO-gCN/PCs (d). e,f) TEM images: Mo:P-gCN/PCs powder (e) and gCN/PCs powder (f).

The shrinkage effect is well observed on the Mo:P-gCN/PCs powder (Figure 4a). This shrinkage effect has been reported in previous works related to similar materials.[20–22] Figure 4g,h shows additional SEM images of Mo:P-gCN/PCs powder measured at different areas with different magnifications. Supplementary SEM images of Mo:P-gCN/PCs powder are provided in Figure S4, Supporting Information.

The higher crystallinity and the defined morphology of Mo:P-gCN/PCs are well evidenced by TEM images (Figure 4e), whereas the TEM image of gCN/PCs (Figure 4f) confirms the lower crystallinity and the amorphous structure of this material. Porous structures are not exhibited in the gCN/PCs powder due to the weak hydrophilicity of PS spheres with the gCN precursor. Very few pores are observed in FTO-gCN/PCs; this sample is not 3D-oriented. Moreover, the material is not mechanically stable on the FTO substrate and collapses easily under any influence. Figure 4i,j shows additional SEM images of FTO-Mo:P-gCN/PCs measured in different areas with different magnifications. Additional SEM images of FTO-Mo:P-gCN/PCs are supplemented in Figure S5, Supporting Information.

The surface topography of Mo:P-gCN/PCs and its chemical composition were investigated by atomic force microscopy (AFM), focused ion beam (FIB), and energy dispersive X ray spectroscopy (EDX) mapping analysis combined with energy dispersive spectroscopy (EDS) analysis, respectively, and their results are shown in **Figure 5**. The 3D AFM image of

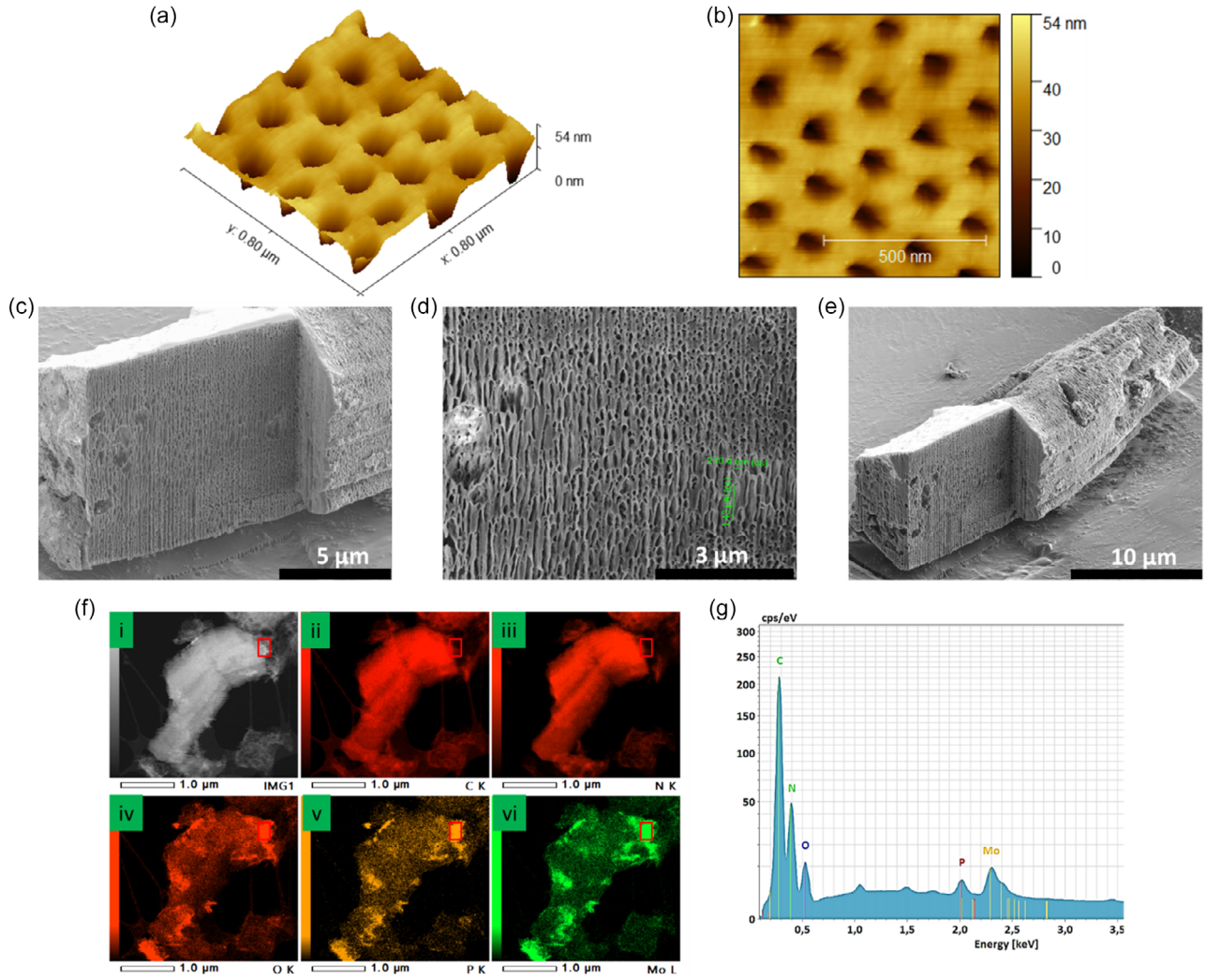

Figure 5. a) 3D AFM images and b) 2D AFM images of FTO-Mo:P/PCs. c–e) FIBM images, f) TEM-EDX, and g) EDS of Mo:P-gCN/PCs powder.

FTO-Mo:P-gCN/PCs (Figure 5a) reveals that several longitudinal regular holes are observed on its surface, and their average depths have been estimated as 38 nm, which is considered the thickness of the Mo:P-gCN/PCs array on FTO substrate. Figure S6, Supporting Information, supplements this observation. The 2D AFM image (Figure 5b) shows regular pores, but the most relevant observation is a dark region across each pore. This confirms the occurrence of a tiny region (with different refractive indices) between the top layer and the layer that follows it; this region is known as an area that blocks the passage of light at specific wavelengths.[20] In that region, the reflected light waves from interfaces between the layers would be scattered at specific wavelengths out of the stack, and the light would be confined radially and guided along the length of the material. This is called the PBG effect.[16,20,24,25] Figure S6, Supporting Information, supplements more observations about the overall topography of the material surface. To support the AFM images, the FIB microscopy images with different magnitudes were measured on the powder PCs, and their results are shown in Figure 5c–e. This measurement helps to show that the porous structure is exhibited on the material's surface and inside the material structure, which is favorable for wave light scattering and confirms the templating effect played by the PS spheres. The PCs grew up following the agglomeration of PS spheres crystal. Additional FIB images supporting the hexagonal 3D porous structure are shown in Figure S7, Supporting Information.

The TEM–EDX elemental mapping has been recorded only on the powder Mo:P-gCN/PCs sample concerning the requirements of the measurement device, and the EDS analysis was also associated (Figure 5f,g, respectively). The TEM–EDX raw map (Figure 5f,i) supplements the fact that the skeleton structure of the PCs grew following the way the PS template has been assembled and agglomerated on its precursor surface. The crystallinity of gCN was also improved by the doping elements (Mo and P atoms) present in its structure, as evidenced by TEM–EDX mapping and its EDS spectra analysis (Figure 5f,g). The EDS spectra of Mo:P-gCN/PCs (Figure 5g) describe the composition of its elements (Table S1, Supporting Information) and indicate

that Mo and P atoms are indeed doped into the structure gCN/PCs. Furthermore, their uniform distribution is illustrated by the TEM–EDX elemental mapping (Figure 5f(v,vi)). In addition to their EDX elemental mappings (Figure 5f(ii,iii), the firm EDS peaks of C and N atoms imply that these atoms carry the building block of the final PCs structure originated from the gCN, meaning that the gCN backbone is not destroyed after the simultaneous effect of the doping and template process. The nonlabeled peaks observed in the EDS spectra (Figure 5g) originated from trace elements in the PS spheres solution and FTO substrate. This observation is well supplemented in Figure S8, Supporting Information.

3.2. FTIR, XRD, BET, TGA, UV–vis DRS Analysis

Figure 6a shows the UV–vis diffuse reflectance spectroscopy absorption spectra of each PCs material, and a comparison is provided with the spectra of their corresponding non-PCs, which means the same materials as the free-PS template. All the samples exhibit broadened absorption peaks in the same region ($\leq$450 nm). Still, the PC samples exhibit higher absorbances than the non-PC; thus, according to the Beer–Lambert law,[26] the incident light is less transmitted in these materials. Hence, the light is more confined inside the materials. This behavior is related to the slow photon effect these materials exhibit and is governed by Bragg's law about light diffraction in 3D materials.[20] Thus, the PBG wavelength of materials has been tuned by controlling the morphology and pore diameter with the help of PS templates. Moreover, its electronic properties must be improved and engaged during light absorption to exploit the light confined inside a material. This has been achieved by Mo:P doping, evidenced by the broadened absorption tail and the blueshift of the light absorption threshold, indicating a *d–d* transition in the sample Mo:P-gNC/PCs (Figure 6a).

Figure 6b shows the Tauc's plot derived from the absorption spectra of each sample for $n = 2$ (direct transition). By the linear interpolation of the tangent of each plot with the *x*-axis, the value of the bandgap energy (E_g) of Mo:P-gCN/PCs was estimated at 2.97 eV against 2.87 eV for gCN/PCs, which is the same as the E_g of pure gCN (Figure S9b, Supporting Information). As the bandgap of pure gCN remains unchanged after the direct shaping of the PS spheres template, this proves that its absorption bands cannot be tuned directly by an opal crystal structure. Consequently, the PBG property derived from PC structures is not directly transferable to pure gCN. Hence, wave light propagation cannot be forbidden in this material. As gCN/PCs keep the same optical properties as pure gCN, they cannot be considered PCs, as evidenced by SEM and TEM results (Figure 4c,d,f). This observation reveals the vital role PMA played at the earlier synthesis stage. The absorption bands of pure gCN have been tuned indirectly by the opal crystal template with the help of PMA, which is used as a mediator. As well as mediating the templating process, PMA subsequently provides the doping effect and presumably the heterojunction formation simultaneously, as reported by Simon et al.[10] The doping effect has been evidenced by the narrowing of the bandgap energy (Mo:P-gCN, $E_g = 2.70$ eV) when the PS spheres crystal template was not involved (Figure S9a, Supporting Information). Narrowing the bandgap of the given photocatalyst can inevitably cause

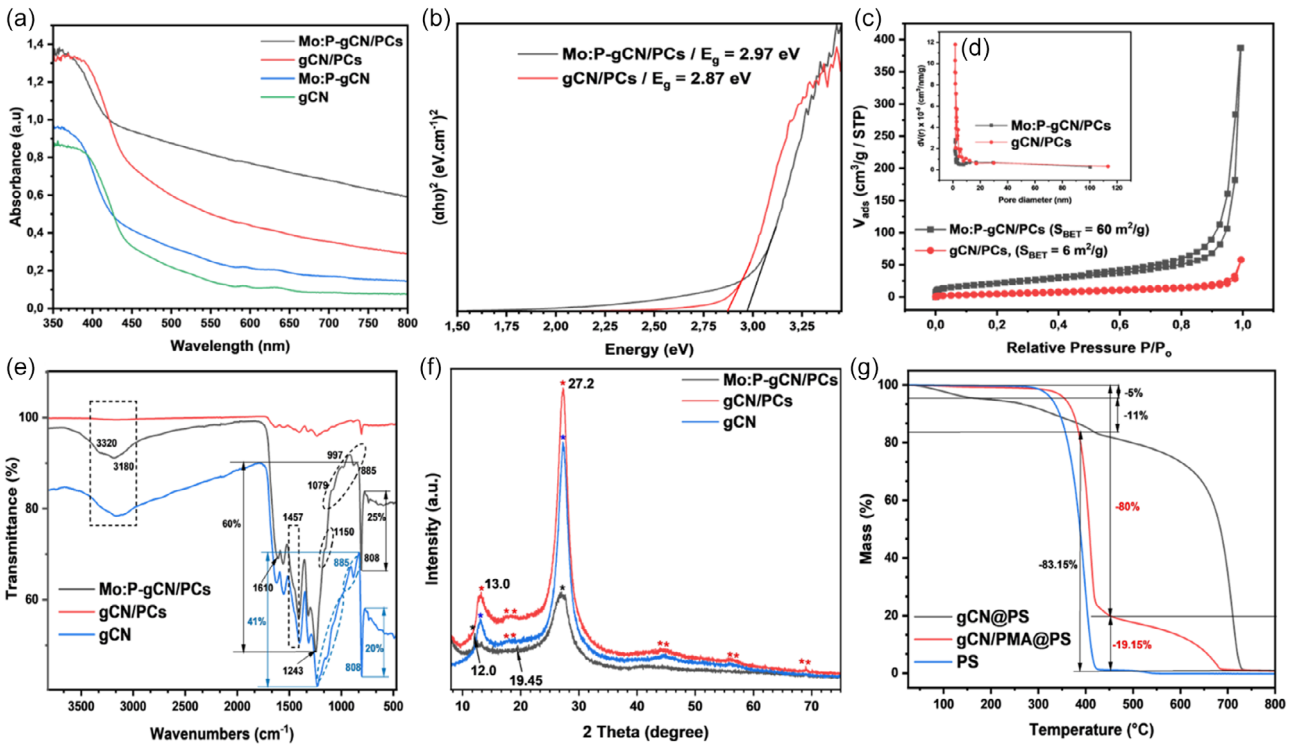

Figure 6. a) UV–vis diffuse absorption spectra, b) Tauc's plot for bandgap energy, c) N_2 adsorption–desorption isotherms, d) pore size distribution plot (inset), e) FTIR spectra, f) XRD patterns, and g) TGA curves.

weakened redox ability, whereas[20] the construction of a hierarchical structure benefits the light–matter interactions because of the multiple scattering of light, thus enhancing light utilization efficiency,[16,20,21] which justifies making doped gCN 3D structures like PCs in this study.

The nitrogen adsorption–desorption isotherms (Figure 6c) reveal that Mo:P-gCN/PCs exhibits a type IV curve of nitrogen adsorption with an H3 hysteresis loop, indicating a mesoporous material with an average pore size of 3.5 nm and pore volume of $0.59\ cm^3\ g^{-1}$ determined from the Barrett Joyner Halenda pore size distribution method (insert Figure 6d). As compared to the size of a single PS sphere particle ($\phi \backsimeq 250$ nm), the significant difference observed with the pore size value comes from the fact that during the formation of the closed-packed gCN/PMA@PS composite, several PS sphere particles have been stuck on the precursor surface from the tiny part of their meniscus (see Figure S3, Supporting Information, to understand this point). In addition, the post-thermal annealing caused a severe volume shrinkage on the powder Mo:P-gCN/PCs, but for the FTO immobilized material, this volume shrinkage is not severely pronounced, hence the advantage of the FTO-Mo:P-gCN/PCs. Mo:P-gCN/PCs shows a Brunauer Emmett Teller (BET) surface area of $60\ m^2\ g^{-1}$, which is 10 times higher than the BET surface area of gCN/PCs ($6\ m^2\ g^{-1}$). As compared to other gCN-modified materials exhibiting higher surface area,[27–29] the photocatalytic performances of Mo:P-gCN/PCs are not ascribed to their surface area but to their improved electronic properties and 3D hierarchical structure. The average pore size for gCN/PCs was 3 nm, and its pore volume was $0.088\ cm^3\ g^{-1}$. The lower value of these previous parameters indicates that the PS sphere particles were not wetted on the gCN precursor due to the hydrophobicity of its surface compared to the PS spheres. As a result, its porosity did not improve and pore volume did not change.

The Fourier transform infrared spectroscopy (FTIR) spectra (Figure 6e and S9c, Supporting Information) disclose better the final chemical structure of the Mo:P-gCN/PCs. Looking at the overall shape of pure gCN and Mo:P-gCN/PCs FTIR spectra, it is observed without any hesitation that the gCN backbone remains in the majority in the final structure of Mo:P-gCN/PCs, confirming that its framework structure carries up the main skeleton of the PCs network; hence, the improved polymeric array's structure is made up of single monomer unit of tri-*s*-triazine. However, additional vibration modes and some changes in vibration intensities have been exhibited in the Mo:P-gCN/PCs IR spectrum, constituting the preservation of its structure. The vibration band at the wave number of $808\ cm^{-1}$ is derived from the breathing vibration of the triazine ring. This peak is commonly attributed to the out-of-plane bending vibration characteristic of heptazine rings.[26,30] This peak is more intense in the Mo:P-gCN/PCs spectrum, meaning that there is a new atom (with lower electronegativity than the N atom) surrounding the electronic cloud of the heptazine unit that makes this vibration easier and more intense. This atom is suspected to be a P atom. The vibration band at $885\ cm^{-1}$ in gCN spectra originating from the cross-linking N—H deformation between CN layers is exhibited as a shoulder in the Mo:P-gCN/PCs spectrum. In the gCN spectrum, this peak is caused by the inadequate condensation of the $–NH_2$ amino groups.[26,31] The weak intensity of this peak in the Mo:P-gCN/PCs spectrum implies the almost total condensation of amino groups, which gives place to forming a new bond with an atom that makes the N—H bond deformation hardly possible. This atom is suspected to be Mo present in the form of an oxide molecule. Additional shoulder peaks at 997 and $1079\ cm^{-1}$ are attributed to the phosphoric acid group's asymmetric and symmetric stretching, respectively, confirming the P-doping into the gCN lattice.[9,32,33] The wrinkled line band observed from 1020 to $1230\ cm^{-1}$ in the gCN spectrum is attributed to the stretching vibration of the bridging secondary amines units (C—NH—C). Mo:P-gCN/PCs spectrum exhibits a shoulder vibration peak at $1150\ cm^{-1}$, but the wrinkled line is not observed, confirming the prolonged condensation of amino groups under the influence of an oxidizing agent, allowing the increase of the polymeric chain and suggesting the presence of Mo atom indirectly bonded with the secondary N from the amino group as previously mentioned. The increase of the polymeric chain is evidenced by the higher transmittance (60%) and the less broadened band peak observed in the region with the wavenumbers between 1243 and $1610\ cm^{-1}$, which are attributed to the stretching vibrations of conjugated heterocyclic rings of tris-*s*-triazine units and secondary amine. The higher intensity in this range stems from the more ordered packing layers of heptazine motifs in the 3D PC array. Around $1457\ cm^{-1}$, the band vibration is sharper for Mo:P-gCN/PCs, implying the implication of the P atom in the heterocyclic conjugated ring of heptazine. There is a broadband vibration with a peak centered at $3180\ cm^{-1}$ with a shoulder at $3320\ cm^{-1}$ assigned to the stretching vibration modes due to the N—H or O—H of the uncondensed/oxidized groups. The FTIR spectrum of gCN/PCs shows that its structure is severely altered due to the vigorous oxidation reaction driven by H_2O_2 under temperature. This demonstrates the protecting and mediator role that PMA played during the synthesizing of the Mo:P-gCN/PCs lattice.

The crystallinity of Mo:P-gCN/PCs was investigated by powder X-ray diffraction (XRD) measurements, and its result was compared to pure gCN, gCN/PCs, and Mo:P-gCN (Figure 6f and S9f, Supporting Information). The diffraction peaks of pure gCN (27.2° and 13.00°), which are also exhibited in the Mo:P-gCN/PCs XRD pattern (27.2° and 12.0°), are consistent with the polymeric structure of the 3D IO crystal arrays and evidence that the gCN backbone is the main skeleton of the final framework. The diffraction peak at 19.45° in Mo:P-gCN/PCs XRD spectrum is consistent with the hexagonal and fcc structure of the PS opal crystal, whose characteristic diffraction peak is well evidenced in Figure S11, Supporting Information. The XRD peak at 27.2 in gCN is not shifted in Mo:P-gCN/PCs, revealing that the interlayer stacking of conjugated aromatic systems (002)[26,34] is typically exhibited in Mo:P-gCN/PCs structure with an average interlayer distance of $d = 0.33$ nm. However, this peak is less sharp and much broader than the same peak in the pure gCN XRD pattern, confirming a change in atoms from conjugated aromatic systems and, hence, the doping effect. As a result, the X-ray beams at this interatomic distance would not be scattered at the same intensity. The broadening of this peak is evidenced by lattice defects in the crystalline structure, and the lower XRD intensity of this peak reveals a dopant size (P atom) more prominent than the host lattice. The XRD peak at 13° in pure gCN corresponding to the intralayer structural stacking of aromatic motifs (100)[26,34] is shifted to 12° in Mo:P-gCN/PCs crystal, leading to

Table 1. Physical parameters and crystalline characteristics.

	Mo:P-gCN/PCs	gCN/PCs	gCN
FWHM[a)] [rad]	4.9	4	3.4
Crystallinity [%]	61	58.7	55.9
E_g [eV][b)]	2.97	2.87	2.87
S_{BET} [$m^{-2}\,g^{-1}$][c)]	60	6	10
P_S [nm][d)]	3.5	3	17
P_V [$cm^{-3}\,g^{-1}$][e)]	0.59	0.088	0.06

[a)]Full width at half maximum; [b)]Bandgap energy; [c)]Specific surface area; [d)]Pore size diameter; [e)]Pore volume.

an increase of the interatomic distance from 0.34 nm to 0.73 nm and revealing Mo atom intercalated in the crystalline lattice. Despite exhibiting a higher FWHM (4.9 rad) according to the Scherrer equation meaning presumably a lower crystallinity, the average crystallinity of Mo:P-gCN/PCs was calculated using the XRD integration method, and the value is recorded in **Table 1**. Mo:P-gCN/PCs possess the highest crystallinity (61%), and its XRD pattern exhibits much more crystalline peaks than XRD patterns of gCN and gCN/PCs. XRD patterns of gCN and gCN/PCs reveal several amorphous phases (Figure S10, Supporting Information). The influence of PS templates on the crystal structure of PCs is also demonstrated through the XRD patterns of free-PS samples (Mo:P-gCN and gCN) compared with that, including PS spheres (Figure S10a–d, Supporting Information). The XRD pattern of gCN is even similar to the XRD pattern of gCN/PCs, confirming that there is no chemical affinity between gCN and PCs.

The thermal stability, the thermal-assisted PS removal, and the supplement chemical compositions of materials were assessed by thermogravimetric analysis (TGA) (Figure 6g, S9d,e, Supporting Information). The close-packed crystal composite gCN/PMA@PS and PS sphere templates were assessed for TGA analysis to get the suitable temperature at which the PS spheres should be removed from the lattice composite, leaving behind the formation of the Mo:P-gCN/PCs. From Figure 6g, one can observe that 450 °C is the suitable temperature to apply for the complete removal of the PS template without any alteration of the gCN framework in the final PCs lattice. Hence, after its formation, the Mo:P-gCN/PCs sample is thermally stable up to 600 °C (Figure S9e, Supporting Information), and it has also been observed that the TGA curves of gCN/PMA@PS and gCN@PMA composites exhibited almost the same shape, demonstrating that, during the gCN/PMA@PS composite formation and Mo:P-gCN/PCs thermal formation, the PS spheres template do not react with the host material, thus it is not chemically bound with the precursor composite (Figure S9d, Supporting Information); it plays only the role of template agent. The Mo:P-gCN/PCs formation takes place at 450 °C in one step with a mass loss of 80% following a simultaneous 100% mass loss at the same temperature by the PS template. After this step, the following represents almost 20% of the mass loss, considered as the residual Mo:P-gCN/PCs with a TGA curve shown in Figure S9e, Supporting Information. The gCN/PCs formation occurs in two steps without following the PS template's mass loss, confirming the PS sphere's weak affinity with gCN and no aggregation and nucleation formation on the gCN surface.

3.3. XPS, PL, Valence Band Spectra, and Electronic Band Structure

Elementary analysis and the electronic chemical state of sample Mo:P-gCN/PCs were investigated by X-ray photoelectronic spectroscopy (XPS) and compared with elements from pure gCN. **Figure 7** shows the high-resolution XPS spectra for each element revealed from the corresponding sample's XPS survey (Figure S12, Supporting Information).

The C 1*s* XPS deconvoluted spectrum in Mo:P-gCN/PCs (Figure 7a) reveals shift peaks compared to C1s XPS peaks in pure gCN corresponding to new chemical interactions that affect the chemical environments of elements. The C 1*s* peaks of Mo:P-gCN/PCs at 284.4 and 288 eV correspond to surface adventitious carbon atoms (C—C) and sp^2-hybridized C atoms in an aromatic ring, respectively. The shift of these peaks and the change in their intensity suggest carbon oxidation, which evidenced the formation of Mo oxide and phosphate ions. The N 1*s* XPS shoulder peak at 399.9 eV is less sharp than the one in pure gCN (399.1 eV), confirming a higher degree of polymerization than pure gCN. The deconvoluted N 1*s* peaks at 398.1 eV are attributed to the interaction of a heteroatom (P or O) with the aromatic ring exhibited by phosphate ions or Mo oxides. The sharp peak of the π electrons in Mo:P-gCN/PCs confirms this observation. The higher resolution XPS also reveals that Mo and P atoms are exhibited as two doublets of $3d_{5/2}$ and $3d_{3/2}$ for the Mo atom and one doublet of $2P_{1/2}$ and $2P_{3/2}$ for the P atom, respectively. The Mo 3*d* doublet located at 234.5 and 231.4 eV might be ascribed to Mo^{4+} connected to oxygen vacancies. In contrast, the Mo 3*d* doublet centered at 235.7 and 232.6 eV is identified as a metallic Mo^{3+} cation responsible for a possible formation of MoP species and considered as one of the active sites toward the efficient HER.[7,10,35] The P 2*p* XPS deconvolution spectrum exhibited only one doublet peak centered at 132.3 and 133.2 eV for P $2p_{3/2}$ and P $2p_{1/2}$, respectively, confirming that P atoms are mainly involved in only two bonding relationships with another specific atom in the lattice. This doublet peak could be ascribed to phosphorus (metal phosphate) bonded to oxygen (P—O) and phosphorus bonded to nitrogen (P—N bonds) with a high oxidation state (+4).

To better understand the photoexcitation mechanism of Mo:P-gCN/PCs, the XPS technique investigated its valence band edge positions (**Figure 8**a) and compared them with those from gCN/PCs and gCN. The experimental energy band structures corresponding to each sample were drawn (Figure 8b). The band structure features induced by the photonic effect of Mo:P-gCN/PCs were demonstrated by comparing its energy band level with that of free-PS material (Mo:P-gCN), which has already been reported.[10] The valence band minimum (VBM) of samples is lower than the VBM of the gCN framework. Simon et al.[10] reported that incorporating PMA into 2D gCN followed by post-thermal treatment slightly lowers its VBM. Thus, its activation energy helps to ease the photon absorption and increase its light absorption ability. Despite its boosting light absorption

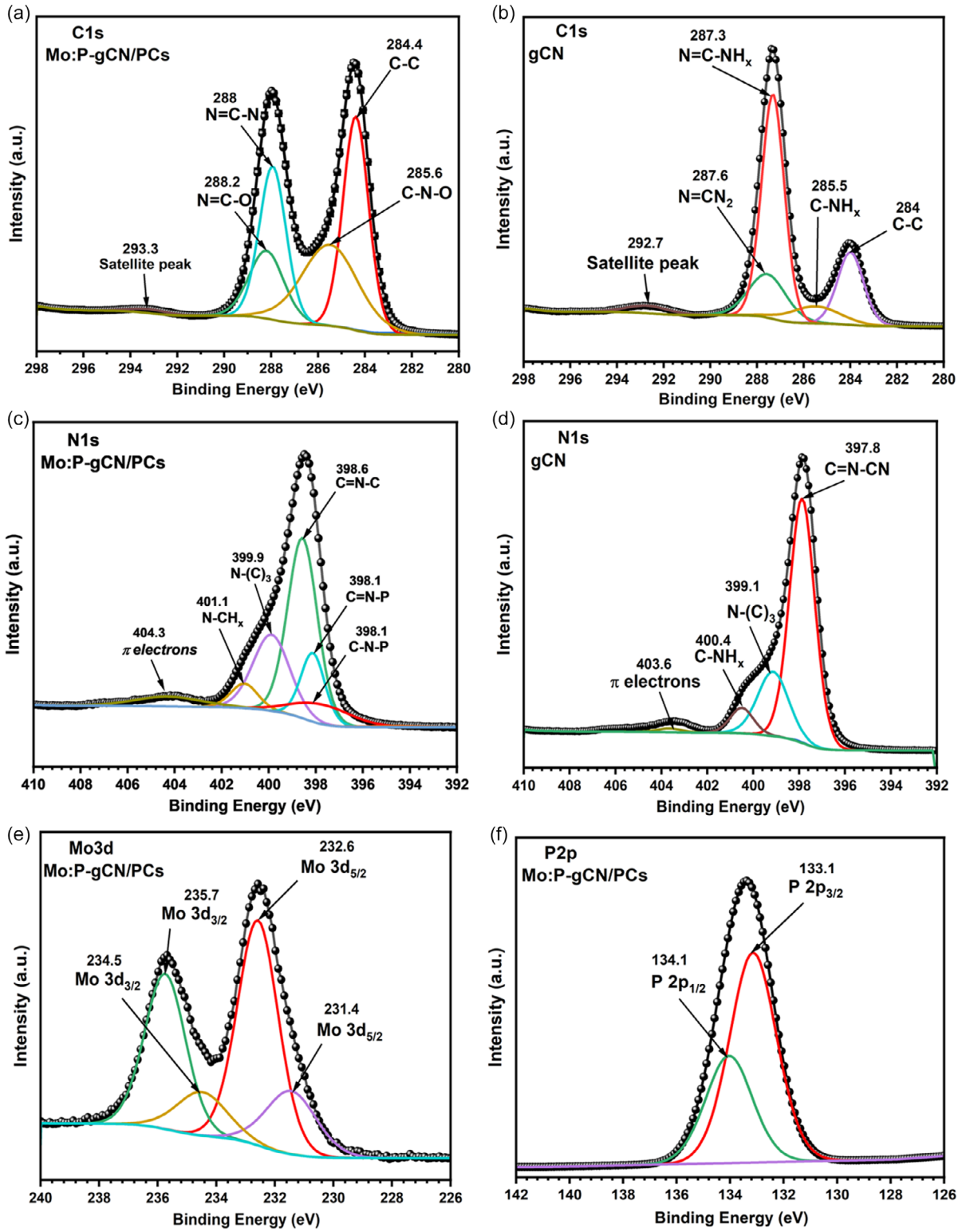

Figure 7. High-resolution deconvoluted XPS spectra of C 1*s* (a, b), N 1*s* (c, d), Mo 3*d* (e), and P 2*p* (f) for Mo:P-gCN/PCs compared to high-resolution deconvoluted XPS spectra of main elements from gCN.

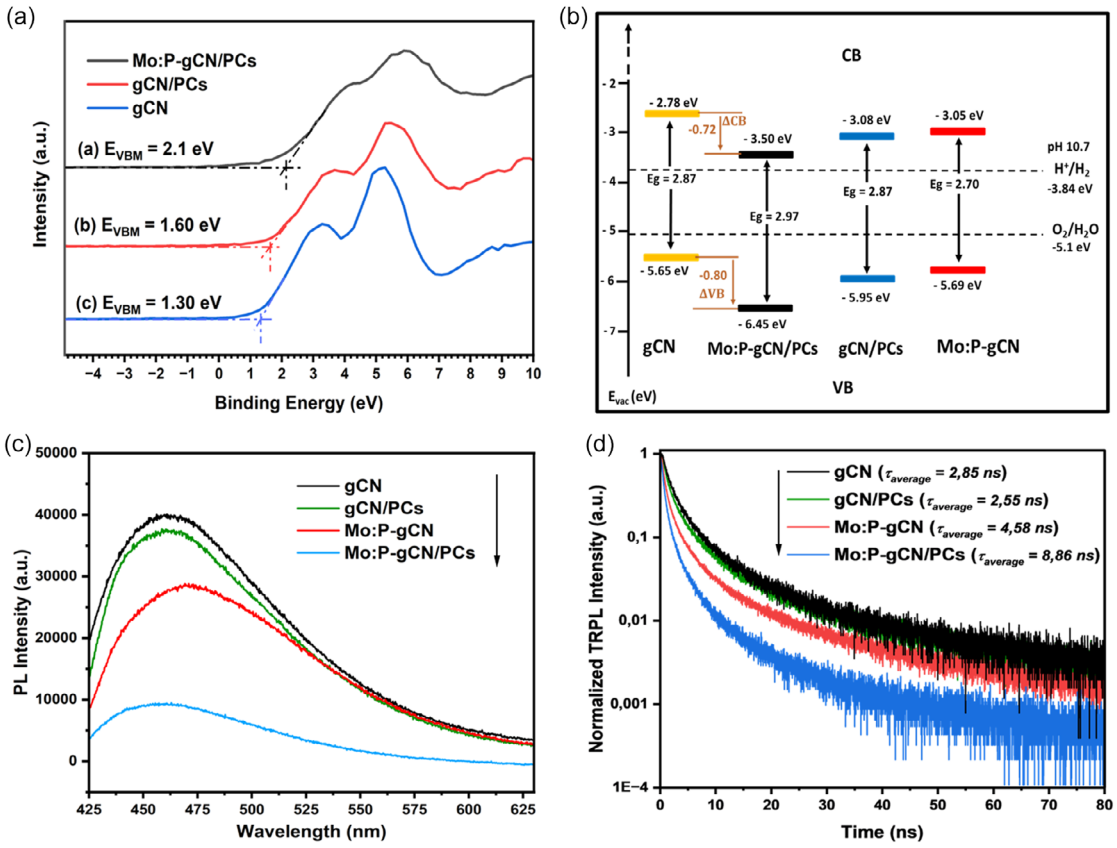

Figure 8. a) XPS valence band spectra, b) electronic band structures, c) steady-state PL spectra, and d) time-resolved transient PL decay spectra.

ability, the valence band (VB) and conduction band (CB) positions are unsuitable for promoting HER; hence, incorporating PMA into the gCN backbone is insufficient to tune the electronic band structure of gCN in favor of efficient HER enhancement. In addition to the doping phenomenon provided by PMA, it is demonstrated that transferring the photonic effect of PCs (exhibited by PS spheres) to the doped gCN results in the accurate tuning of the electronic band's structure to the potential that would easily promote HER better than OER (Figure 8b). Thus, Mo:P-gCN/PCs exhibit a VB position located very far away from the OER potential, and its CB position is located very near to the HER potential, matching well for photocatalytic hydrogen production.

To evaluate the extent of charge transfer/separation and to estimate the energy-wasteful recombination in the pure gCN and the PCs products, photoluminescence (PL) spectra and PL lifetime of the powdered samples (Figure 8c,d) have been examined in the range of 420–650 nm with an excitation wavelength of 407 nm and transferred onto Si Wafer for measurements. A strong PL emission was observed at around 460 nm for the pure gCN due to the radiative recombination of charge carriers. This PL emission peak was slightly suppressed for the gCN/PCs sample. However, further suppression of this peak is observed for Mo:P-gCN, indicating that the bicontinuous framework could create a large electron trapping center.[36,37] Despite the lower specific surface area, The PL emission was strongly suppressed for Mo:P-gCN/PCs (Table 1). This observation demonstrates that in addition to the doping phenomenon, providing a 3D porous structure to gCN material could help tune its electronic band structure and further improve its optical and photonic properties, which are being used to enhance HER. The PL spectrum of Mo:P-gCN/PCs showed the obvious blueshift of the PL emission peak, and the broadened tail emission observed in other samples above the PL maximum wavelength is also suppressed, demonstrating the PBG effect exhibited by the doped gCN PCs (Figure 8c) aiming to stop or attenuated the radiative propagation of specific frequencies. To investigate the transfer dynamics of the charge carriers under irradiation and underlying the emission quenching, time-resolved photoluminescence (TRPL) decay spectra were recorded, as shown in Figure 8d. The lifetime of Mo:P-gCN/PCs TRPL became longer (8.86 ns) due to the stop-band suppression, indicating the opening of an additional channel of electron transfer from Mo:P-gCN to Mo:P-gCN/PCs.[37,38] Mo:P-gCN/PCs TRPL quenching and its longer lifetime indicate a new electron transfer route in another less radiative quenching mode, leading to energy transfer and implying the improved lifetime of excited species in this material structure.

4. Application: Photocatalytic HER and PEC Response

To estimate the light-to-energy conversion of the Mo:P-gCN/PCs sample, its photoactivity has been evaluated through a photocatalytic reactor setup for hydrogen production (Figure S16,

Supporting Information) and compared with other samples. Hence, the intrinsic photocatalytic activities of the as-prepared samples were evaluated by monitoring the HER via the water-splitting reaction under visible light irradiation. **Figure 9**c shows screening HER tests performed in the small glass reactions for only shorter irradiation times (see SI for the experimental part). These tests were beneficial in giving an idea about the photoactivity of each sample and predicting the reaction behavior before running for longer irradiation time in the big reactor. From this test, it appears that the amount of hydrogen produced is about 2050 μmol g^{-1} over 6 h of irradiation, corresponding to a reaction rate of about 342 μmol g^{-1} h^{-1} against 300 μmol g^{-1} h^{-1} for Mo:P-gCN/PCs. Pure gCN and gCN/PCs had already predicted their weak activity from the screening test (Figure 9c). However, running an HER for shorter irradiation is inefficient in demonstrating the reliability and stability of a photocatalytic system for large-scale applications. Figure 9a displays the pressure control concerning hydrogen produced inside the big reaction chamber for longer irradiation time. Higher pressure evolution is observed for Mo:P-gCN/PCs over irradiation time, implying a higher hydrogen volume produced. The gas chromatograph quantified the gas produced from the reaction chamber, the volume percentage of H_2 evolved was recorded, and its amount was calculated from the slope of the graph pressure and the ideal gas equation following previous works.[10,39] The plot of H_2 evolved for longer irradiation time is shown in Figure 9b.

The reaction rate was 750 μmol g^{-1} h^{-1} for Mo:P-gCN/PCs against 625, 150, and 167 μmol g^{-1} h^{-1} for Mo:P-gCN, gCN/PCs and gCN, respectively. Hence, it is demonstrated that Mo:P-gCN/PCs exhibited higher light-to-energy conversion than the other samples, proving that by combining the doping effect with the slow photon effect of PCs, it is there possible to significantly tune the electronic band structure and optical properties of gCN and thus improving its photocatalytic activities. Furthermore, to demonstrate the photocatalytic activity over longer irradiation times, the HER from the reaction chamber (Figure 9b) also describes the stability of the photocatalytic system integrating Mo:P-gCN/PCs. For over 120 h of irradiation, Mo:P-gCN/PCs material is not deactivated compared to gCN and gCN/PCs, which exhibit a deactivation reaction.

For PEC investigations, the sample FTO-Mo:P-gCN/PCs and FTO-gCN/PCs were used as working electrodes (see SI). These powder samples were immobilized onto FTO, as mentioned in Section 2. In addition, transient photocurrent and the electrochemical linear sweep voltammetry (LSV) analysis can also reveal the charge transfer and separation efficiency. Figure 9e shows the chronoamperometry (CA) of the photocurrent density collected at 1.23 V and demonstrates that Mo:P-gCN/PCs displays a rapid response for periodic light on–off cycles despite the low current density as compared to that one from gCN/PCs (Figure S13, Supporting Information). Higher photocurrent density implies higher utilization of visible light and more efficient photocarrier transportation. The light source for this measurement was near the visible range, which explains why the current density of Mo:P-gCN/PCs was lower than gCN/PCs. Table S2, Supporting Information, describes the reaction conditions applied to the photocatalytic HER. The current density observed for Mo:P-gCN/PCs did not follow the photocatalytic hydrogen

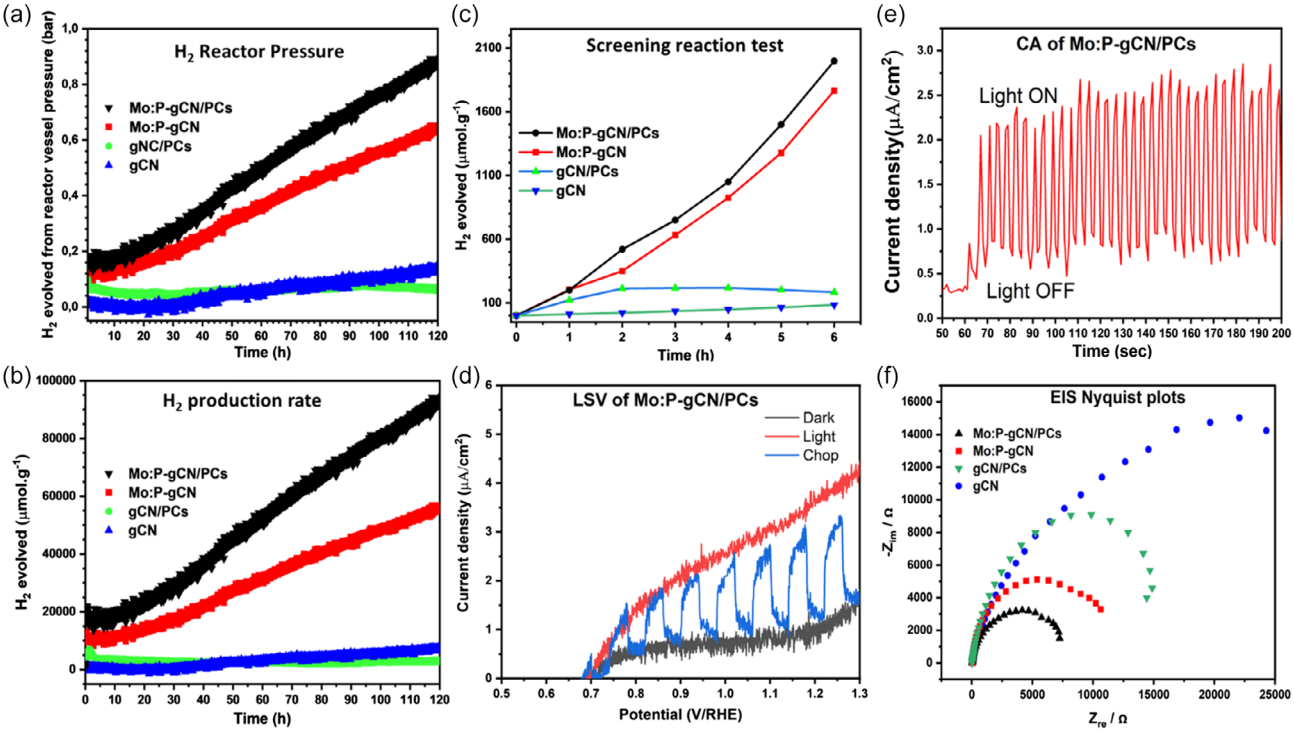

Figure 9. a) Reactor pressure control for long-time photocatalytic HER, b) hydrogen evolved from the reaction chamber over long-time photocatalytic reaction, c) screening of photocatalysts, d) LSV, e) transient photocurrent responses, and f) the Nyquist plots of electrochemical impedance spectroscopy.

evolution rate in Figure 9b,c. The main reason for this situation is the difference in the reaction conditions between the electrochemical and photocatalytic parts. The photocatalytic reaction was carried out with a 300 W Xe lamp with a 395 nm cutoff filter and a temperature control system. The light source was used without any temperature control for the PEC measurements. gCN/PCs sample is more sensitive to visible light than Mo:P-gCN/PCs under an applied potential but was not sensitive at all under visible only. In contrast, the Mo:P-gCN/PCs sample is sensitive under applied potential and visible light. The easy photocurrent response of Mo:P-gCN/PCs reveals at least the evidence of efficient charge generation and separation, which is well evidenced by PL measurements. The Nyquist plot of EIS shown in Figure 9f supplements the easy charge transfer for sample Mo:P-gCN/PCs. Performed under dark conditions, the Nyquist plot of pure gCN has been compared to that from Mo:P-gCN and Mo:P-gCN/PCs to elucidate the effect of contact resistance on photocatalytic performances. All the samples show semicircle curves in the tested frequency region, which mainly reflected the resistance of interfacial charge transfer impedance of active material.[40,41] Its smallest Nyquist curves diameter demonstrates that the internal charge transfer resistance of Mo:P-gCN/PCs is lower than the other samples, suggesting that this 3D material greatly enhanced the electron transport speed, leading to the best photocatalytic performance. Thus, the above results indicate that the photonic effect of the PS template has been transferred to Mo:P-gCN, resulting in promoted charge transfer and inhibiting charge carriers from fast recombination, consistent with its highest hydrogen evolution rate. However, the reaction stability of Mo:P-gCN/PCs is well described on the LSV and CA of the recycled sample. Figure S14, Supporting Information, shows that the recycled Mo:P-gCN/PCs give a photocurrent response, whereas the recycled gCN/PCs sample does not (Figure S14c,d, Supporting Information). The photocatalytic cycle and reusability test were performed cyclically to supplement the stability of the photocatalytic system. Hence, the system exhibits its photoactivity after several reaction cycles despite the change in reaction rate. By showing the photocatalytic cycle and reusability cycle test (Figure S17, Supporting Information), we can demonstrate the extent of the stability and reusability of our material for large-scale applications. The optoelectronic properties of Mo:P-gCN/PCs are additionally demonstrated by the LSV measurements following electrochemical water oxidation potential (Figure 9d, Supporting Information), which show the redox properties of this material and the recycled one (Figure S14a,b, Supporting Information) with periodic light ON-OFF cycles. Thus, these results indicate that Mo:P-gCN/PCs promotes charge transfer and inhibits charge carriers from fast recombination; therefore, it could be used to improve light-to-energy conversion. The unchanged texture and morphology and the less change in structural composition after the photocatalytic HER ensure the prolonged activity and stability of Mo:P-gCN/PCs over long-term HER (Figure S18, S19, and S20, Supporting Information).

5. Conclusion and Outlooks

When harvesting the light energy and converting it into its storage form for long-term use, we may ultimately need to mimic natural photosynthesis. The effectiveness of the light-to-energy conversion is dedicated to the material's ability to absorb radiative wavelengths, generate photo-generated charges (electrons and holes), and suppress their rapid recombination for promoting prolonged light-driven chemical reactions resulting in its conversion into energy carrier. Despite its ability to easily initiate the light-driven water-splitting reaction, gCN exhibits several drawbacks. Still, it provides at least one of the best chemical frameworks for synthesizing highly efficient catalyst materials to enhance light harvesting. Hence, this work describes for the first time a unique strategy involving POM and PS opals in three steps that results simultaneously in the P-doping effect and slow photon effect to gCN lattice, resulting in the substantial improvement of its electronic band structure and its optoelectronic properties. We have demonstrated the effect of Mo:P codoping by demonstrating the effect of PS sphere crystals on the structural, electronic, PEC, and optical performances of modified gCN with direct application on the photocatalytic HER from the water-splitting reaction. It has been demonstrated that a fine Mo:P-gCN/PCs powder structure is obtained when there is a perfect nucleation and PS aggregation between PS template spheres and precursor composite, meaning that the chemical composition of gCN/PMA composite should play in favor of a suitable chemical affinity with PS spheres. For the immobilized sample (FTO-Mo:P-gCN/PCs), a well 3D-orientated close-packed PS opal is required. The final Mo:P-gCN/PCs exhibited an HER activity (750 $\mu mol\, g^{-1}\, h^{-1}$), which is 1.2 times higher than Mo:P-gCN (625 $\mu mol\, g^{-1}\, h^{-1}$), demonstrating that the slow photon effect exhibited by the PS opal crystal has been transferred to the final PCs resulting in the improvement of its photocatalytic active. The apparent quantum efficiency for Mo:P-gCN/PCs was calculated as 1.3% compared to 0.7% for Mo:P-gCN. The photoactivity of pure gCN and gCN/PCs was found to be very low, demonstrating that the simultaneous P-doping followed by the slow photon effect can improve the electronic and optical properties of gCN and shape the morphology of gCN material has a positive impact on the final structure and properties. Despite the goals achieved, it should be mentioned that the photoactivity of final Mo:P-gCN/PCs remains weak compared to other materials.[42,43] But we must say that these materials, whose enormously improved light harvesting, are mainly composed of multicomponent semiconductors or very heavy and complex molecules comprising several units from different monomers. This study demonstrated how it could substantially improve the light-to-energy conversion only with a single material polymer consisting of units from a unique monomer. Our results open new opportunities for using gCN with other POMs to synthesize other gCN/POM composite precursors for further assembly with PS opals to prepare other PCs materials. We started with the PMA as a representative for POM materials and obtained good HER activity when a certain amount is loaded onto gCN. We guess that a screening of other POM materials might enhance the photocatalytic activity further and this might also lead to more active PCs. Also, a facile and efficient photocatalytic activity could be obtained by varying the light source (Figure S15, Supporting Information) and testing different applications like CO_2 reduction or water decontamination.

Supporting Information

Supporting Information is available from the Wiley Online Library or from the author.

Acknowledgements

The authors acknowledge the funding from the Deutsche Forschungsgemeinschaft (DFG, German Research Foundation) under Germany's Excellence Strategy—EXC 2008/1 (UniSysCat)—390540038 and the Einstein Centre of Catalysis (EC^2) of the Technische Universität Berlin. S.Y.D. thanks the Berlin International Graduate School of Natural Sciences and Engineering (BIG-NSE) for the doctoral training program. He gratefully acknowledges the significant contribution of the Elsa Neumann Stiftung of the Berlin state for the scholarship provided. The authors also gratefully thank Ulrich Gernert, Christoph Fahrenson, Ron Justin Simke J., Christian Günther, and Sören Selve from the ZELMI team of TU-Berlin for their assistance with the spectroscopy measurements and all the technical staff of our laboratories, especially Gabriele Vetter, Maria Unterweger, Astrid Müller-Klaude, and Christina Eichenauer. Basundhara Dasgupta from TU-berlin is also gratefully acknowledged for contributing to EIS measurements.

Conflict of Interest

There are no conflict to declare.

Author Contributions

Simon Y. Djoko T.: Conceptualization (equal); Formal analysis (lead); Investigation (lead); Methodology (lead); Software (lead); Visualization (lead); Writing—original draft (lead); Writing—review and editing (lead). **Sunil Kwon**: Formal analysis (supporting); Investigation (supporting). **Prasenjit Das**: Formal analysis (supporting); Investigation (supporting); Writing—review and editing (equal). **Vincent Weigelt**: Formal analysis (supporting); Investigation (supporting); **Warisha Tahir**: Formal analysis (supporting); Investigation (supporting). **Babu Radhakrishnan**: Formal analysis (supporting); Investigation (supporting). **Klaus Schwarzburg**: Formal analysis (supporting); Investigation (supporting). **Arne Thomas**: Resources (equal); Validation (equal); Writing—review and editing (equal). **Michael Schwarze**: Formal analysis (supporting); Project administration (supporting); Validation (equal); Writing—review and editing (equal). **Reinhard Schomäcker**: Conceptualization (equal); Project administration (lead); Resources (lead); Supervision (lead); Validation (equal); Writing—review and editing (equal).

Data Availability Statement

The data that support the findings of this study are available from the corresponding author upon reasonable request.

Keywords

3D microporous structures, doping, light-to-energy conversion, photonic crystals, slow photon effect

Received: June 20, 2024
Revised: September 3, 2024
Published online: September 30, 2024

[1] A. Naseri, M. Samadi, A. Pourjavadi, A. Z. Moshfegh, S. Ramakrishna, *Graphitic Carbon Nitride (g-C3N4)-Based Photocatalysts for Solar Hydrogen Generation: Recent Advances and Future Development Directions*, Vol. *5*, Royal Society of Chemistry **2017**, pp. 23406–23433.
[2] J. Fu, J. Yu, C. Jiang, B. Cheng, *Adv. Energy Mater.* **2018**, *8*, 1701503.
[3] W. J. Ong, L. L. Tan, Y. H. Ng, S. T. Yong, S. P. Chai, *Chem. Rev.* **2016**, *116*, 7159.
[4] L. Jiang, X. Yuan, Y. Pan, J. Liang, G. Zeng, Z. Wu, H. Wang, *Appl. Catal. B* **2017**, *217*, 388.
[5] A. Indra, A. Acharjya, P. W. Menezes, C. Merschjann, D. Hollmann, M. Schwarze, M. Aktas, A. Friedrich, S. Lochbrunner, A. Thomas, M. Driess, *Angew. Chem., Int. Ed.* **2017**, *56*, 1653.
[6] Y. Gu, A. Wu, Y. Jiao, H. Zheng, X. Wang, Y. Xie, L. Wang, C. Tian, H. Fu, *Angew. Chem., Int. Ed.* **2021**, *60*, 6673.
[7] J. Sen Li, S. Zhang, J. Q. Sha, H. Wang, M. Z. Liu, L. X. Kong, G. D. Liu, *ACS Appl. Mater. Interfaces* **2018**, *10*, 17140.
[8] Y. Li, L. Cai, Q. Huang, J. Liu, R. Tang, W. Zhou, *Nanoscale Res. Lett.* **2020**, *15*, 16.
[9] B. Liu, L. Ye, R. Wang, J. Yang, Y. Zhang, R. Guan, L. Tian, X. Chen, *ACS Appl. Mater. Interfaces* **2018**, *10*, 4001.
[10] S. Y. Djoko, T. E. Njoyim, T. A. D. Nguyen, J. Yang, H. Küçükkeçeci, E. M. Kutorglo, B. Radhakrishnan, K. Schwarzburg, S. Huseyinova, P. Das, M. Tasbihi, M. Schwarze, A. Thomas, R. Schomäcker, *Catal. Sci. Technol.* **2023**, *14*, 2114.
[11] T. Maka, D. N. Chigrin, S. G. Romanov, C. M. Sotomayor Torres, *Prog. Electromagn. Res.* **2003**, *41*, 307.
[12] R. Yew, S. K. Karuturi, H. H. Tan, C. Jagadish, *Nanostructured Photoelectrodes via Template-Assisted Fabrication, Semiconductors and Semimetals*, 1st ed, Elsevier Inc., **2017**, vol *97*.
[13] V. P. Bykov, *JETP* **1972**, *35*, 239.
[14] L. Zhang, C. Baumanis, L. Robben, T. Kandiel, D. Bahnemann, *Small* **2011**, *7*, 2714.
[15] X. Chen, J. Ye, S. Ouyang, T. Kako, Z. Li, Z. Zou, *ACS Nano* **2011**, *5*, 4310.
[16] J. Cai, M. Wu, Y. Wang, H. Zhang, M. Meng, Y. Tian, X. Li, J. Zhang, L. Zheng, J. Gong, *Chem* **2017**, *2*, 877.
[17] Z. Huang, L. Fang, W. Dong, Y. Liu, Z. Kang, *J. Nanosci. Nanotechnol.* **2014**, *14*, 4156.
[18] M. Zhou, J. Bao, Y. Xu, J. Zhang, J. Xie, M. Guan, C. Wang, L. Wen, Y. Lei, Y. Xie, *ACS Nano* **2014**, *8*, 7088.
[19] P. Varma, L. Alvares Rodrigues, Y. Lianqing, D. A. Reddy, *Appl. Surf. Sci.* **2023**, *624*, 157143.
[20] Y. Chen, L. Li, Q. Xu, W. Chen, Y. Dong, J. Fan, D. Ma, *Sol. RRL* **2021**, *5*, 2000541.
[21] F. Liu, Z. Gao, J. Hu, Y. Meng, S. Zhang, B. Tang, *J. Mater. Sci.* **2019**, *54*, 10609.
[22] H. Li, J. F. Wang, G. Vienneau, G. Bin Zhu, X. G. Wang, J. Robichaud, B. L. Su, Y. Djaoued, *RSC Adv.* **2017**, *7*, 46406.
[23] E. A. Gaulding, G. Liu, C. T. Chen, L. Löbbert, A. Li, G. Segev, J. Eichhorn, S. Aloni, A. M. Schwartzberg, I. D. Sharp, F. M. Toma, *J. Mater. Chem. A. Mater.* **2017**, *5*, 11601.
[24] H. E. Ruda, N. Matsuura, *Springer Handbook of Electronic and Photonic Materials* **2017**, p. 1013.
[25] G. I. N. Waterhouse, A. K. Wahab, M. Al-Oufi, V. Jovic, D. H. Anjum, D. Sun-Waterhouse, J. Llorca, H. Idriss, *Sci. Rep.* **2013**, *3*, 2849.
[26] A. Majdoub, M. Majdoub, S. Rafqah, H. Zaitan, *Environ. Sci. Pollut. Res.* **2023**, *30*, 85940.
[27] K. Li, Y. Lin, Y. Zhang, M. Xu, L. Liu, F. Liu, *J. Mater. Chem. C* **2019**, *7*, 13211.
[28] S. Bag, K. Roy, C. S. Gopinath, C. R. Raj, *ACS Appl. Mater. Interfaces* **2014**, *6*, 2692.

[29] S. Y. Tameu Djoko, H. Bashiri, E. T. Njoyim, M. Arabameri, S. Djepang, A. K. Tamo, S. Laminsi, M. Tasbihi, M. Schwarze, R. Schomäcker, *J. Photochem. Photobiol. A* **2020**, *398*, 112596.
[30] Y. Ezhumalai, P. Kumaresan, T. Jayapalan, *Graphite Carbon Nitride Photocatal. New Perspect. IntechOpen (Rijeka)*, **2022**.
[31] N. D. Shcherban, P. Mäki-Arvela, A. Aho, S. A. Sergiienko, P. S. Yaremov, K. Eränen, D. Y. Murzin, *Catal. Sci. Technol.* **2018**, *8*, 2928.
[32] S. Ansari, M. Ansari, M. Cho, *Sci. Rep.* **2016**, *6*, 27713.
[33] J. Y. Tang, D. Yang, W. G. Zhou, R. T. Guo, W. G. Pan, C. Y. Huang, *J. Catal.* **2019**, *370*, 79.
[34] S. Sunasee, K. H. Leong, K. T. Wong, G. Lee, S. Pichiah, I. W. Nah, B. H. Jeon, Y. Yoon, M. Jang, *Environ. Sci. Pollut. Res.* **2019**, *26*, 1082.
[35] M. Wang, C. Ye, M. Xu, S. Bao, *Nano Res.* **2018**, *11*, 4728.
[36] Q. Han, B. Wang, Y. Zhao, C. Hu, L. Qu, *Angew. Chem.* **2015**, *127*, 11595.
[37] X. Wang, K. Maeda, X. Chen, K. Takanabe, K. Domen, Y. Hou, X. Fu, M. Antonietti, *J. Am. Chem. Soc* **2009**, *131*, 1680.
[38] M. Barth, A. Gruber, F. Cichos, *Phys. Rev. B* **2005**, *72*, 085129.
[39] M. Schwarze, D. Stellmach, M. Schröder, K. Kailasam, R. Reske, A. Thomas, R. Schomäcker, *Phys. Chem. Chem. Phys.* **2013**, *15*, 3466.
[40] P. Das, G. Chakraborty, J. Yang, J. Roeser, H. Küçükkeçeci, A. D. Nguyen, M. Schwarze, J. Gabriel, C. Penschke, S. Du, V. Weigelt, I. E. Khalil, J. Schmidt, P. Saalfrank, M. Oschatz, J. Rabeah, R. Schomäcker, F. Emmerling, A. Thomas, *ChemRxiv* **2024**. https://doi.org/10.26434/chemrxiv-2024-t696j.
[41] H. Han, T. Song, E. K. Lee, A. Devadoss, Y. Jeon, J. Ha, Y. C. Chung, Y. M. Choi, Y. G. Jung, U. Paik, *ACS Nano* **2012**, *6*, 8308.
[42] J. Yang, S. Ghosh, J. Roeser, A. Acharjya, C. Penschke, Y. Tsutsui, J. Rabeah, T. Wang, S. Y. Djoko Tameu, M. Y. Ye, J. Grüneberg, S. Li, C. Li, R. Schomäcker, R. Van De Krol, S. Seki, P. Saalfrank, A. Thomas, *Nat. Commun.* **2022**, *13*, 6317.
[43] E. M. Kutorglo, M. Schwarze, A. D. Nguyen, S. D. Tameu, S. Huseyinova, M. Tasbihi, O. Görke, M. Primbs, M. Šoóš, R. Schomäcker, *RSC Adv.* **2023**, *13*, 24038.